



JGR Space Physics

RESEARCH ARTICLE

10.1029/2021JA030101

Key Points:

- The electromagnetic ion cyclotron (EMIC) wave diffusion process causes significant precipitation of tens of keV protons, particularly in the afternoon to midnight sector
- Energetic precipitating proton scattered by EMIC wave further impact ionosphere-thermosphere and contribute to the ionization in E/F regions
- EMIC waves produce large proton precipitation, changing ionospheric electrodynamics and feeding back to the magnetospheric dynamics

Correspondence to:

Y. Yu, yiqunyu17@gmail.com

Citation:

Tian, X., Yu, Y., Zhu, M., Ma, L., Cao, J., PR, S., et al. (2022). Effects of EMIC wave-driven proton precipitation on the ionosphere. *Journal of Geophysical Research: Space Physics*, 127, e2021JA030101. https://doi. org/10.1029/2021JA030101

Received 4 NOV 2021 Accepted 10 JAN 2022

© 2022. American Geophysical Union. All Rights Reserved.

Effects of EMIC Wave-Driven Proton Precipitation on the Ionosphere

Xingbin Tian^{1,2}, Yiqun Yu^{1,2}, Minghui Zhu^{1,2}, Longxing Ma^{1,2}, Jinbin Cao^{1,2}, Shreedevi PR¹, Vania K. Jordanova³, and Stanley C. Solomon⁴

¹School of Space and Environment, Beihang University, Beijing, China, ²Key Laboratory of Space Environment Monitoring and Information Processing, Ministry of Industry and Information Technology, Beijing, China, ³Space Science and Application, Los Alamos National Laboratory, Los Alamos, NM, USA, ⁴High Altitude Observatory, National Center for Atmospheric Research, Boulder, CO, USA

Abstract We investigate the proton precipitation caused by electromagnetic ion cyclotron (EMIC) waves and its impact on the ionosphere with the self-consistent ring current-atmosphere interactions model (RAM-SCBE) coupled with an ionospheric particle transport model Global Airglow (GLOW). The EMIC wave diffusion process causes significant precipitation of tens of keV protons, particularly in the afternoon to midnight sector. These precipitating energetic protons further impact the ionosphere-thermosphere and contribute to the ionization in the E/F regions. The integrated auroral conductance is significantly enhanced in the dusk-to-midnight sector. Although the EMIC waves do not directly interact with the ring current electrons, after the EMIC wave scattering included in the model, remarkable changes are found in the global distribution of precipitating electron flux. This means that the addition of proton precipitation driven by EMIC waves results in feedback effects on the ring current electron dynamics through the circulation system. Validation is also conducted by comparing the simulated precipitation flux and ionospheric electron density with observations.

1. Introduction

Particle precipitation from the plasma sheet is one important energy source for the ionosphere and plays an important role in modulating the dynamics of the ionospheric system and causing aurora (Chen et al., 2005, 2015; Chen & Schulz, 2001; Creutzberg et al., 1988; Galand et al., 2001; Hardy et al., 1989; Immel et al., 2002; Lui et al., 1977; Lyons, 1992; Su et al., 2017; Ridley et al., 2004; Thorne et al., 2010). Newell et al. (2009) found that precipitating electrons contribute 63%/57% and ions 14%/15% to the diffuse energy flux into the ionosphere during quiet/active times. In previous studies, Hardy et al. (1989) found that the relative contribution of ions to the total energy flux is on average about 15% of that of electrons during geomagnetically disturbed periods but it is comparable during quiescent times (Creutzberg et al., 1988). Although the electron precipitation appears to be the major energy source into the ionosphere at most of the time, the precipitating ions cannot be neglected, particularly in the dusk sector (Newell et al., 2009; Tian et al., 2020; Zhu et al., 2021).

The precipitation of the magnetospheric ions results from many physical processes in the magnetosphere, including pitch angle diffusion associated with the electromagnetic ion cyclotron (EMIC) waves (Jordanova et al., 2001, 2007; Liang et al., 2014; Ni et al., 2016; Sakaguchi et al., 2008; Shreedevi et al., 2021; Su et al., 2011; Yuan et al., 2010) and field line curvature (FLC) scattering (Ebihara & Ejiri, 2003; Chen et al., 2019; Yu et al., 2020). Studies have shown that the FLC scattering contributes to the ring current decay (Ebihara et al., 2011) and produces proton precipitations in the larger-L regions where the field lines are more stretching and the scattering is more efficient (Chen et al., 2019; Young et al., 2008; Yu et al., 2020; Zhu et al., 2021). On the other hand, the EMIC waves can cause significant proton precipitation in the postnoon-to-midnight sector and induce proton aurora (Fuselier et al., 2004; Jordanova et al., 2007). Yuan et al. (2014) reported a proton precipitation event induced by EMIC waves. They calculated the electron density in the ionospheric E region with the precipitating protons and found that the E region electron density is significantly enhanced, consistent with the GPS-observed TEC. These studies imply the importance of EMIC waves in inducing proton precipitation and the subsequent impact on the ionosphere. However, a global-wide investigation of the effects of the wave-driven proton precipitation on the ionosphere is still lacking. Therefore, this study will examine the global distribution of

TIAN ET AL. 1 of 15



proton precipitation in association with EMIC waves and the consequent effects on ionospheric electrodynamics, especially the conductivity.

The ionospheric auroral conductivity, as a result of the precipitating particle impact, is of great importance in the geospace circulation. It plays an essential role in determining the electric potential that controls the plasma convection in both the ionosphere and magnetosphere (Lotko et al., 2014; Ridley et al., 2004). As the calculation of the conductivity profile involves various parameters of both the ionosphere and thermosphere, it is not trivial. Therefore, a classic technique in global models is adopting the Robinson's relation (Robinson et al., 1987) or Galand & Richmond relation (Galand & Richmond, 2001) to specify the auroral conductance related to precipitating electrons or protons respectively (Chen et al., 2019; Chen, Lemon, Guild, et al., 2015; Chen, Lemon, Orlova, et al., 2015; Raeder et al., 2001; Yu et al., 2016, 2017; Zhang et al., 2015; Zhu et al., 2021). Despite the efficiency, while using the above simple relations, the height profile of the conductivity cannot be explicitly revealed and the physical interactions within the ionosphere-thermosphere are not self-consistently treated. Recently, Yu et al. (2018) integrated a ring current kinetic model RAM-SCBE (Jordanova et al., 2010; Yu et al., 2017) with a two-stream electron transport model GLOW (Solomon, 2017) to investigate the chain effects from the substorm-time electron precipitation to subsequent impact on the ionosphere. It is found that as substorm injections recurrently bring in energetic plasma sources, pitch angle scattering due to chorus waves results in substantial electron precipitation, often accompanied by an enhanced tail above 30 keV. This drives an intermittent enhancement of Pedersen conductivity below 90 km, in addition to the primary conductivity layer around 110 km. In their study, the incident particle impact is solely from precipitating electrons.

In this study, we will incorporate the proton precipitation associated with EMIC waves into the same model to examine its influence on ionosphere conductivity. As presented below, we will first analyze an ion precipitation event when the EMIC wave activity is observed by ground stations and proton precipitation is detected by satellites, and then carry out global simulations to uncover the global distributions of ion precipitation and responses in the ionospheric conductivity. Comparisons with incoherent scatter radar measurements are also conducted for validation.

2. Data

The precipitation data of electrons and protons are obtained from the NOAA's Polar Orbiting Environmental Satellites (NOAA-15 and MetOp-02) (Evans & Greer, 2004). The POES satellites are Sun-synchronous low-altitude polar-orbiting spacecraft and have identical instrumentation. The orbit of POES spacecraft is \sim 800 km altitudes, \sim 102 min orbital period. We use the particle measurements from the Medium Energy Proton and Electron Detector (MEPED) (Galand & Evans, 2000) that measures high-energy integral electron fluxes in three energy bands and proton fluxes in six energy bands. The detector consists of two telescopes, which point approximately parallel (0° telescope, detecting precipitating particles) and perpendicular (90° telescope, detecting the geomagnetically trapped particles) to the local magnetic field line, respectively. In this paper, we mainly use the precipitating particles flux data measured by 0° telescope and with a time resolution of 16 s.

The ground observations data of geomagnetic pulsations is obtained from the Pinawa (PINA) and Thief River Falls (THRF) stations of the Canadian Array for Realtime Investigations of Magnetic Activity (CARISMA) (Mann et al., 2008). The power spectrum density (PSD) is calculated from geomagnetic pulsation data with a sampling frequency of 20 Hz using Fast Fourier Transform.

The ionospheric electron density is obtained from the Millstone Hill incoherent scatter radar (ISR). With observations of the zenith, the ISR provides the ionospheric electron density data from 90 to 300 km with a height resolution of a few km. The related Pedersen and Hall conductivities can be calculated by using the observed electron density data with the help of MSIS/IRI models (Bilitza et al., 2014; Picone et al., 2002).

3. Model Description

We use a coupled ring current-ionosphere model to simulate particle precipitation and subsequent effects on the ionosphere. The ring current dynamics and precipitation loss are solved by the RAM-SCBE model (Jordanova et al., 2006; Yu et al., 2017; Zaharia et al., 2006) and the height-dependent responses in the ionosphere due to

TIAN ET AL. 2 of 15



the incident particles are determined by the GLOW model (Bailey et al., 2002; Solomon, 2017). Details of these models are described below.

3.1. RAM-SCBE Model

By solving the bounce-averaged Fokker-Planck equation $F_l(R, \phi, E, \alpha)$ (Equation 1), the kinetic Ring current Atmosphere interactions Model model (RAM) computes the distribution functions for the ring current particles (H^+ , He^+ , O^+ , and electrons) in the inner magnetosphere. The particle distribution functions are pitch angle-resolved (0°–90°), at all magnetic local times (MLTs) within the radial distance of 2–6.5 R_E in the magnetic equatorial plane, and kinetic energy from 0.15 to 400 keV.

$$\frac{\partial F_{l}}{\partial t} + \frac{1}{R_{o}^{2}} \frac{\partial}{\partial R_{o}} \left(R_{o}^{2} \langle \frac{dR_{o}}{dt} \rangle F_{l} \right) + \frac{\partial}{\partial \phi} \left(\langle \frac{d\phi}{dt} \rangle F_{l} \right)
+ \frac{1}{\gamma p} \frac{\partial}{\partial E} \left(\gamma p \langle \frac{dE}{dt} \rangle F_{l} \right) + \frac{1}{h \mu_{o}} \frac{\partial}{\partial \mu_{o}} \left(h \mu_{o} \langle \frac{d\mu_{o}}{dt} \rangle F_{l} \right) = \langle \left(\frac{\partial F_{l}}{\partial t} \right)_{loss} \rangle$$
(1)

Where R_o is the radial distance in the magnetic equatorial plane, E is the kinetic energy of the particles, μ_o is the cosine of the equatorial pitch angle α , ϕ is the geomagnetic east longitude, p is the relativistic momentum of the particle, γ is the Lorentz factor, and $h(\mu_o)$ is proportional to the bounce path length in the magnetic field (Jordanova et al., 2006).

Solving the temporal evolution of the phase space distribution function requires time-dependent plasma boundary conditions, magnetic field, and electric field. The plasma boundary conditions in the model (i.e., $6.5R_E$) are specified by the plasma flux data obtained from the Los Alamos National Laboratory (LANL)/Synchronous Orbit Particle Analyzer (SOPA) and Magnetospheric plasma analyzer (MPA) instruments. The measured ion fluxes are decoupled into three major ring current ion species according to the statistical formulation by Young et al. (1982). The magnetic field needed in the RAM model is self-consistently estimated from the force-balanced 3D equilibrium magnetic code (Zaharia et al., 2006). The electric field is derived from the field-aligned currents, calculated from the pressure and magnetic gradient in the inner magnetosphere (Vasyliunas, 1970), and ionospheric conductance that is determined by both magnetospheric particle precipitation and solar irradiance (Yu et al., 2017).

The losses of both ring current electrons and ions are included in the RAM-SCBE model. The electron loss processes incorporated in the model include the pitch angle scattering by chorus/hiss waves at regions outside/inside the plasmapause (Albert, 2005; Glauert et al., 2014; Horne et al., 2013; Jordanova et al., 2016; Yu et al., 2016). The ion loss processes specified in the model include adiabatic loss, charge exchange with hydrogen geocorona and pitch angle diffusion associated with EMIC wave scattering (Jordanova et al., 2001; Shreedevi et al., 2021; Zhu et al., 2021). The pitch angle diffusion processes of both electrons and ions are solved by a diffusion equation, in which pitch angle diffusion coefficients are demanded. In this study, the diffusion coefficients for electrons are determined by the quasilinear theory using the PADIE code (Albert, 2005; Horne et al., 2013; Glauert et al., 2014). The diffusion coefficients for ions are calculated similarly with the quasi-linear theory following Ni et al. (2015) and Cao et al. (2016). The statistical global distribution of EMIC wave intensity was derived by Saikin et al. (2016) based on Van Allen Probes measurement. Details of how the diffusion processes due to chorus/hiss waves and EMIC waves are implemented in the model can be found in Yu et al. (2016), Shreedevi et al. (2021), and Zhu et al. (2021). Following these scattering processes, particles entering loss cones precipitate down to the atmosphere.

3.2. Global Airglow (GLOW) Model

The GLOW model (Solomon, 2017) takes into account the photoionization due to the solar radiation, the impact from both precipitating electrons and protons and the secondary photoelectrons generated in the photoionization. The model solves two-stream Boltzmann equations to model the electron transport through the atmosphere. The ionization rates due to precipitating protons are computed based on the parameterization in Fang et al. (2010, 2013). The model determines altitude profiles of emission rates, ionization rates, electron density and conductivity from \sim 70 km to \sim 600 km (Bailey et al., 2002; McGranaghan et al., 2015; Solomon, 2017). The GLOW model takes inputs, such as neutral density and temperature, from the empirical thermosphere model (i.e., NRLMSISE-00) (Picone et al., 2002).

TIAN ET AL. 3 of 15



In this study, the GLOW model is integrated to the ring current model RAM-SCBE (Yu et al., 2018) and receives the precipitating flux of both electrons and protons from the RAM-SCBE model. The altitude profiles of electron density and both Hall and Pedersen conductivities from the GLOW model are then integrated over height to yield the conductance, which is further used to determine the convective electric potential, needed by the RAM-SCBE model.

4. Observations

The 17 March 2013 storm event is driven by a coronal mass ejection (CME) with an interplanetary shock impinging the magnetosphere at 06:00 Universal Time (UT), as shown in Figures 1a and 1b. The SYM-H index reaches its minimum of –100 nT around 10:30 UT and further decreases to –132 nT at 20:00 UT. After an initial fast recovery, the storm experiences a long recovery phase. Following the storm sudden commencement (SSC), the AE index increases to above 500 nT and remains at a high level, suggesting substantial substorm injections during the storm main phase.

Figure 1c shows the positions of two NOAA satellites projected down to the surface and two ground-based stations (PINA and THRF stations of CARISMA). At \sim 22:40 UT, the NOAA-15 spacecraft was located in the post-noon sector around MLT \sim 16, and the MetOp-02 spacecraft was in the pre-midnight sector around MLT \sim 21. The two stations were positioned closely, near the trajectory of NOAA-15 at MLAT \sim 58 and MLT \sim 15.7. Figures 1d and 1e display the power spectrum density (PSD) of geomagnetic pulsation at the two stations. The He^+ and O^+ ion gyrofrequencies are calculated with the TS05 model (Tsyganenko & Sitnov, 2005) at the equatorial plane after mapping the location of the ground stations to the equator. From 21:30 to 23:00 UT, the PSD at the frequency of \sim 0.5 Hz (i.e., the band of Pc1 waves) was between the O^+ and He^+ ion gyrofrequency. This is a signature of the He-band EMIC waves at the equatorial plane (Sakaguchi et al., 2008; Yuan et al., 2012), which may be generated in the magnetosphere and propagate down to the ground. Around 22:45 UT, the NOAA-15 satellite flew over the PINA and THRF stations and detected a remarkable enhancement in the precipitating proton flux. The observed proton flux of 30–80 keV is about one order of magnitude larger than the precipitating electron flux, while that of 100–200 keV is more or less comparable to the electron flux, as shown in Figure 1f. Given the close locations between the NOAA-15 satellite and the two stations, the large proton precipitation is likely induced by the EMIC waves in the magnetosphere.

MetOp-02 at MLT ~ 20.7 also detected large proton precipitation of 30–80 keV, comparable to that of electrons of 30–100 keV as shown in Figure 1g. The precipitating flux of the higher-energy protons (80–250 keV) is even 10 times larger than that of the electrons (100–300 keV). Unfortunately, observational facilities near this space-craft trajectory were too limited to measure the wave activity. Nevertheless, based on these observations, we can infer that proton precipitation over 30 keV provides either as much as or more energy deposition than the electron precipitation does to the dusk sector ionosphere. The proton precipitation is one of the important energy sources for the ionosphere in these regions. To examine the global distribution of ion precipitation in association with EMIC waves and subsequent influence on the ionosphere, we next use the RAM-SCBE model coupled with the GLOW model to simulate this event.

5. Simulation Results

Since the wave activity occurred during the well-known 17 March 2013 magnetic storm, we simulate the whole-day storm event to reveal both temporal evolution and spatial distribution of the particle precipitation and ionospheric responses.

5.1. EMIC Wave Induced Proton Precipitation

Similar to previous studies (Shreedevi et al., 2021; Zhu et al., 2021), we adopt the statistical EMIC wave model derived based on many-year observations of the Van Allen Probes and categorized by the AE index (Saikin et al., 2016). According to the AE index at a particular time, we interpolate the statistical model onto the spatial grids in the model. Figures 2a and 2b show the global distribution of both H-band and He-band EMIC wave

TIAN ET AL. 4 of 15

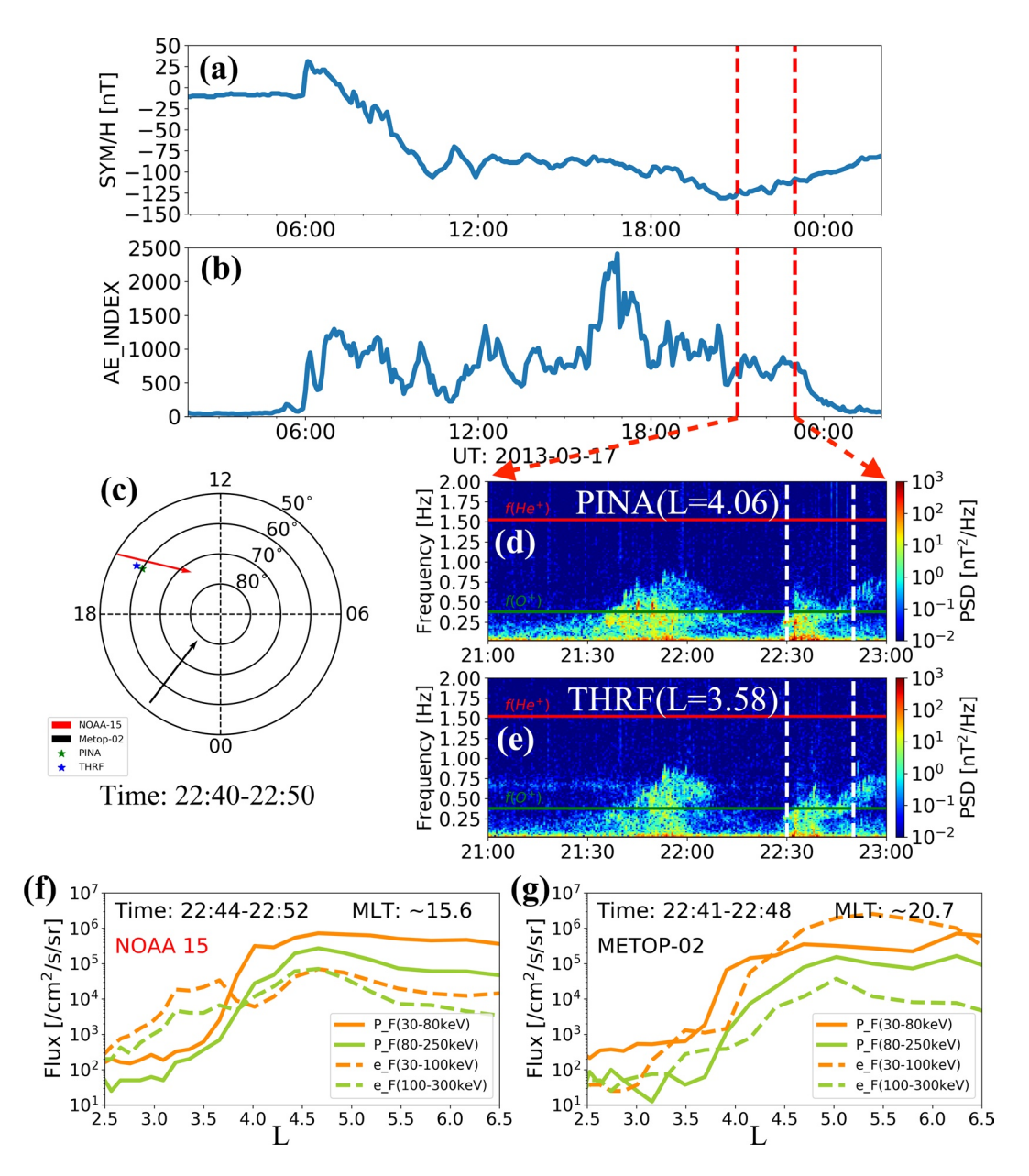


Figure 1. (a) SYM-H index and (b) AE index on 17 March 2013. (c) The location of PINA and THRF ground-based magnetometer and the orbit of NOAA-15 (red line) and MetOp-02 (black line). (d and e) The power spectrum density of the D component (geomagnetic east-west) of geomagnetic pulsation is measured by the PINA and THRF stations. The red and green lines indicate the He^+ and O^+ ion gyrofrequencies at the equatorial plane, respectively. (f and g)The observations of proton and electron precipitation flux over different energy ranges from the NOAA-15 and MetOp-02.

intensity at 22:40 UT. It can be seen that the H-band EMIC wave predominately appears in the prenoon-to-dusk sector with its peak intensity in the dusk, while the He-band wave occurs in a similar region but peaks on the dayside. For L < 6 Re, this statistical distribution of He-band EMIC wave is similar to that of the recent work by Jun et al. (2021), such that both show the peak occurrence in the noon-to-dusk sector (i.e., 12–21 MLT). But the used statistical distribution of H-band EMIC wave shows wider MLT coverage than that of Jun et al. (2021), which mainly occurs in the noon sector (i.e., 10–14 MLT). Based on such wave intensity, the pitch angle diffusion coefficient $\langle D_{\alpha\alpha} \rangle$ is calculated from quasi-linear theory, as a function of energy and pitch angle. Figures 2c and 2d show such coefficients at MLT = 18 and L = 4. These coefficients suggest how fast the particles

TIAN ET AL. 5 of 15



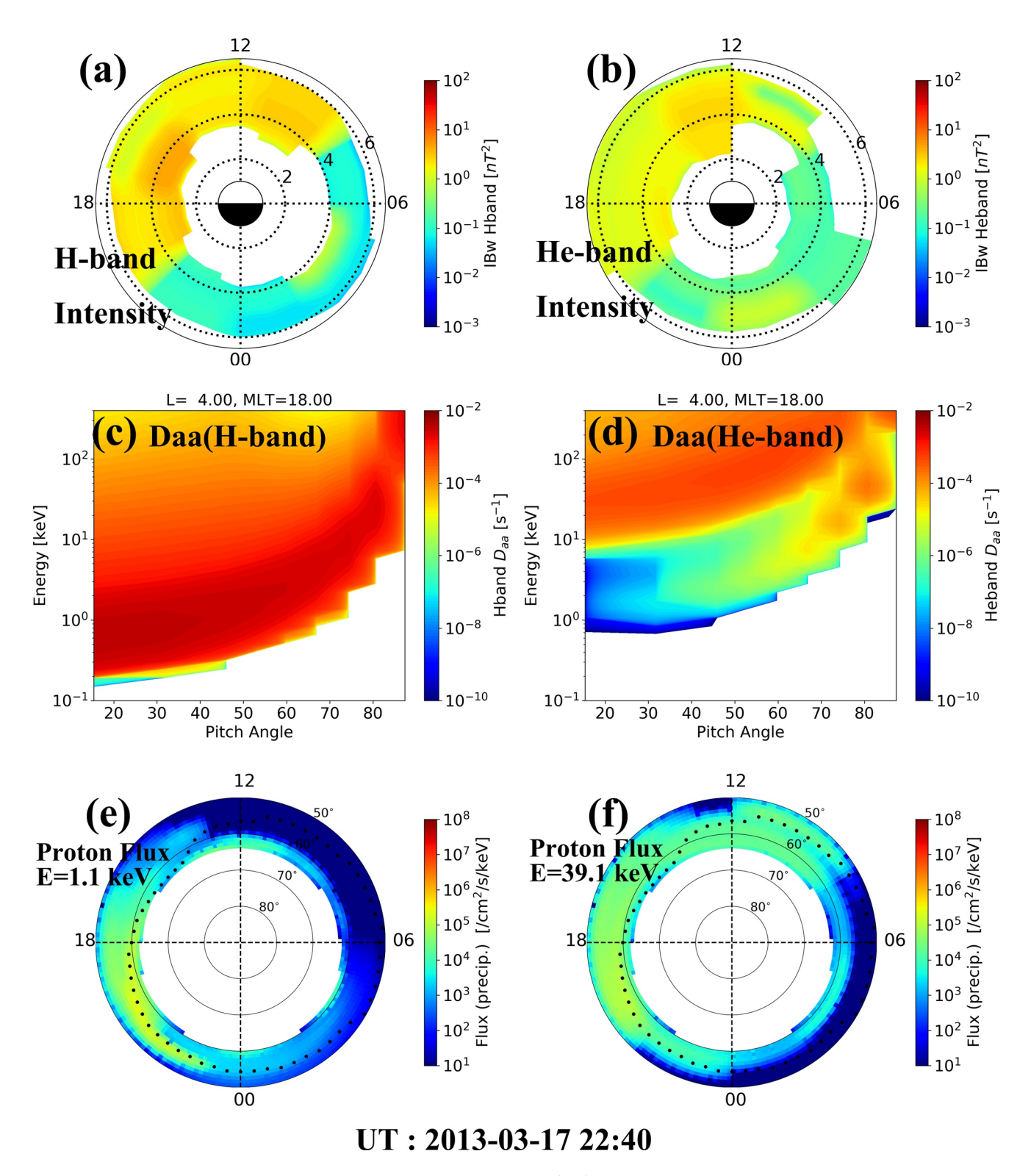


Figure 2. (a and b) The EMIC wave magnetic field density IBw, the diffusion coefficient $\langle D_{\alpha\alpha} \rangle$ as a function of energy and pitch angle at MLT = 18 and L=4 and the precipitating proton flux at different energies (E=1 and 40 keV) at ionospheric altitudes from the simulations with EMIC waves at 22:40 UT. (a and c) H-band EMIC wave; (b and d) He-band EMIC wave. The black dots indicate the latitude of the plasmapause location mapped from the magnetosphere.

TIAN ET AL. 6 of 15



can be resonantly scattered by waves. The H-band EMIC waves appear to be capable of scattering low-energy (E < 1 keV) ions while the He-band EMIC waves can interact with ions with higher energies (E > 10 keV). Figures 2e and 2f show the precipitating proton flux at E = 1 and 40 keV over the ionosphere. The black dots represent the plasmapause boundary mapped from the magnetosphere. Intense precipitation occurs in the noon-to-midnight sector in the vicinity of the plasmapause, where EMIC waves are mostly active. The precipitation of low-energy protons mainly occurs in the dusk-to-midnight sector, while the higher-energy mainly occurs in the prenoon-to-midnight sector. In the presence of EMIC wave scattering, the proton precipitation at all energy ranges enhances and extends widely to almost all MLT sectors.

5.2. Ionospheric Responses

We further analyze the precipitating flux spectra of both electrons and protons at MLT = 18 and MLAT = 60° (L ~ 4 Re), and the corresponding responses in the altitudinal ionosphere. Two simulations, with the EMIC waves included or excluded, are carried out for comparison. The simulation without EMIC wave scattering shows that the storm-time electron precipitation flux mainly exhibits a power-law distribution, with larger flux at lower energies, as shown in Figure 3b. At some instances, a high-energy tail emerges above 10 keV, for example, around 15:00 UT. In contrast, the proton precipitation flux is nearly negligible (Figure 3a). On the other hand, when the EMIC wave is included in the simulation, the proton precipitating flux of E < 100 keV is significantly enhanced (Figure 3f). This is because the H-band EMIC wave can diffuse ions of lower energy (0.1-a few keV) and the He-band EMIC wave is more effective in ion scattering of E > 10 keV. Compared to the other simulation, the precipitating flux of lower-energy electrons is suppressed in this case. But that of 3 < E < 40 keV electron is occasionally enhanced largely during 12:00-18:00 UT and after 21:00 UT, as seen in Figure 3g. Such a high-energy tail in the electron flux spectrum is found to be related to the elongated plasmasphere plume rotating into the afternoon-dusk sector (the time evolution of the plasmapause position is shown in Figure 4g), in which the hiss waves can effectively diffuse these tens of keV electrons. In this high-energy tail, the enhancement shows a dispersed feature. Higher-energy electrons precipitate first, followed by lower-energy electron precipitation. The red curve represents the energy flux. The protons seem to carry as much energy flux as electrons at this location, except in periods when intermittent energetic electrons are precipitated away from the plasmaspheric plume. Comparing the two simulations, we note that the precipitating electron flux is significantly altered after the inclusion of EMIC waves. Although EMIC waves do not directly interact with the ring current electrons, the proton precipitation into the ionosphere and consequent changes in the ionosphere must have caused feedback effects in the circulation system, which then further changes the electron dynamics in the magnetosphere.

Driven by the above differential fluxes, we then examine the ionospheric responses as simulated by the GLOW model. Figures 3c-3e and show the temporal evolution of the height-dependent electron density, Pedersen and Hall conductivities at MLT = 18 and MLAT = 60° from both simulations. In the simulation with EMIC waves excluded, the electron density in the E/F region is around 10^{5} cm⁻³ while the low altitudes (<100 km) region is weakly enhanced around 15:00-16:00 UT and after 23:00 UT. The Pedersen conductivity displays two distinct layers around 120 and 85 km respectively. The low-altitude conductivity layer is associated with energetic precipitating electrons that can penetrate deeper to lower altitudes and produce larger electron density (Hosokawa & Ogawa, 2010; Yu et al., 2018). The high-energy tails (>10 keV) in the electron flux spectra shown in Figure 3g provide the necessary sources.

On the other hand, when the EMIC waves are included and considerable precipitating protons travel downward to the ionosphere, the ionospheric electron density and ionization rate change significantly. The electron density in the E/F region above 100 km is enhanced by an order of magnitude. Such large ionization lasts throughout the entire storm time. This is because the proton precipitation is more persistent at this location during storm time. According to Fang et al. (2010, 2013), protons of 10-100 keV can induce large ionization (> $1.0 \times 10^3/s$) for altitude from ~200 km down to ~100 km, while electrons of the same energy can yield large ionization as deep as 120-80 km. The enhanced ionization below 100 km after 12:00 UT is thus mostly attributed to the precipitating electrons of 3-40 keV, as shown in Figure 3g. The dispersed enhancement of the D region electron density is well correlated with the dispersed energy tail in the electron flux spectrum. Meanwhile, both conductivities in the E and F regions are greatly amplified. The Pedersen conductivity exhibits a primary peak at 120 km that is more sustained than in the previous simulation. This is likely the result of continuous proton precipitation. The sublayer conductivity at 80 km shows quasi-periodic dispersed enhancement, in accordance with the electron

TIAN ET AL. 7 of 15



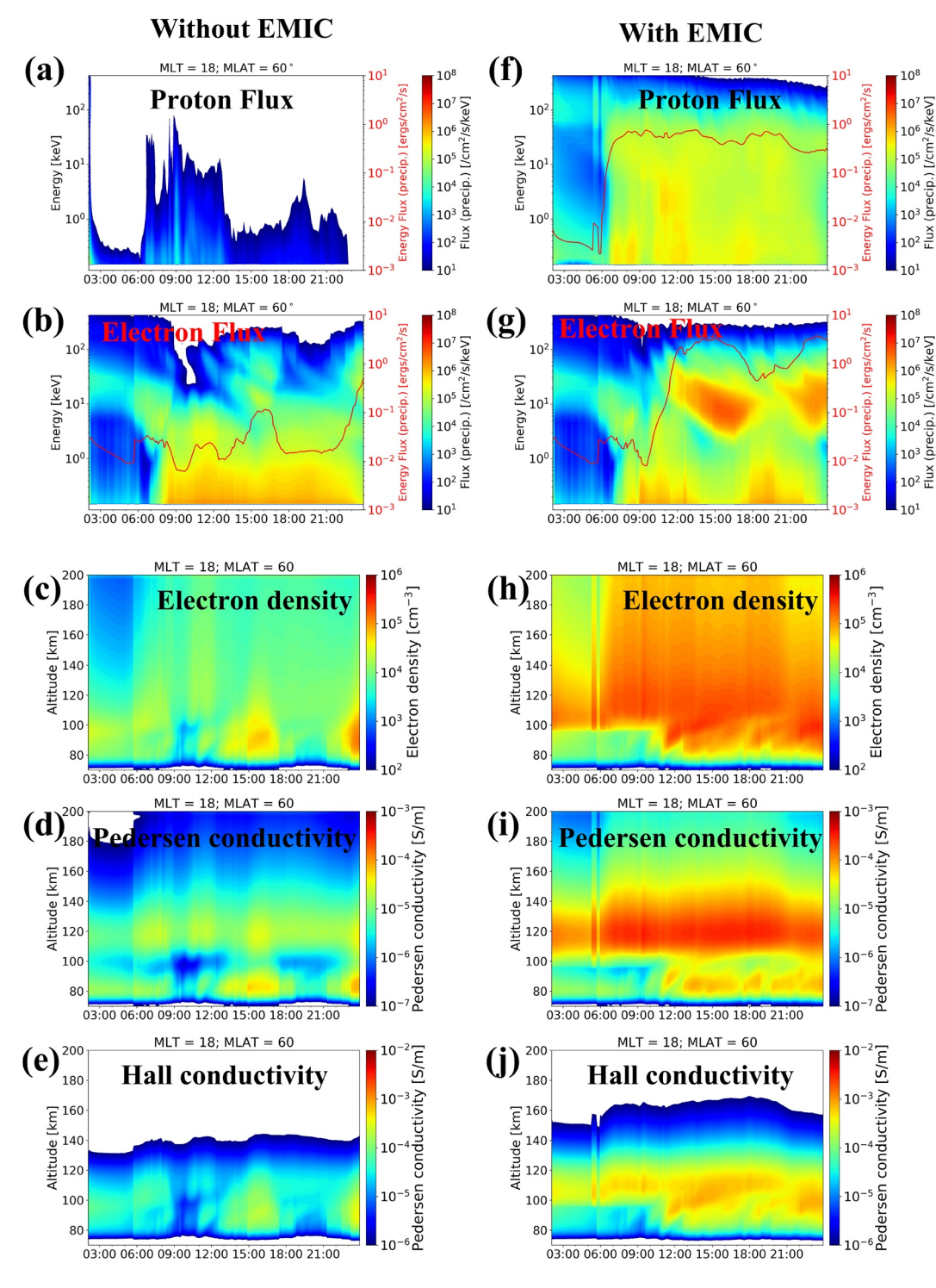


Figure 3. The time evolution of precipitating proton and electron flux spectra and the height-dependent electron density, ionization rate, Pedersen conductivity and Hall conductivity at MLAT = 60° and MLT = 18 obtained from two simulations (a–e) without EMIC waves; (f–j) with EMIC waves. The red lines represent the precipitating energy flux.

precipitation in the high-energy tail. The Hall conductivity primarily peaks around 110 km, with its large intensity sometimes extending below 97 km after 11:00 UT and also showing a two-layer structure temporally. Hosokawa and Ogawa (2010) pointed out that there is a characteristic altitude at ~97 km, where the ions are completely constrained to neutrality and the motion of electrons is partially disturbed by the collision with the

TIAN ET AL. 8 of 15



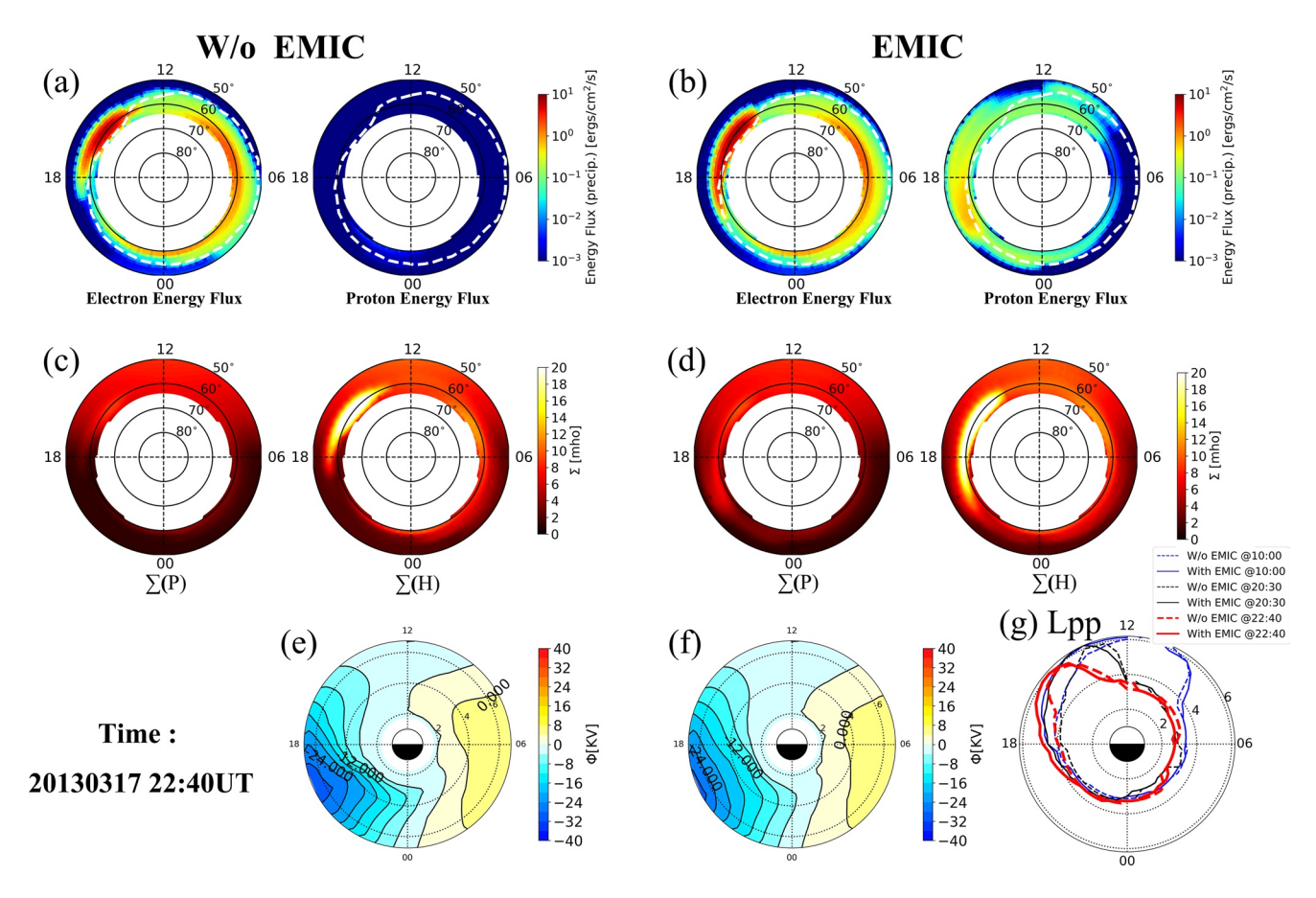


Figure 4. The energy flux (top row), the ionosphere Pedersen and Hall conductance (middle row) at the ionosphere altitude and the electric potential and plasmapause location (bottom row) in the equator at 22:40 UT were obtained from two simulations. (a, c and e): without EMIC waves; (b, d and f): with EMIC waves. The energy flux and conductance panels use the geomagnetic latitude, whereas the electric potential and plasmapause location panels use L-values as the radial coordinate.

neutrals. This characteristic altitude determines the boundary between the ions-dominating conductivity layer and the electrons-dominating conductivity layer.

Figure 4 shows the precipitating energy flux and height-integrated conductance over the ionosphere, and the mapped electric potential at the equatorial plane at 22:40 UT. When the EMIC waves are not included, the precipitation energy flux of protons is very low, while the precipitating electron energy flux is predominantly high in the dawn sector as well as in the post-noon sector. As a result, both Pedersen and Hall conductances are large in the midnight-to-dawn sector and the noon-to-dusk sector (Figure 4c). However, when the effect of EMIC waves is included in the simulation (Figure 4b), the proton energy flux increases in the dusk-to-midnight sector and the conductance is remarkably augmented over there, substantially replenishing the low conductance region in the dusk sector (Figure 4d). The dusk sector Pedersen conductance reaches 15 mhos and the Hall conductance is even higher. After comparing the two simulations, we find that the electric potential is notably altered such as the potential is weaker in the new simulation, especially in the dusk sector. This could influence the particle dynamics in the magnetosphere. The less-skewed and less-concentrated potential contours in the new simulation tend to result in a smaller electric field in the afternoon-to-dusk sector and hence slower drift velocity of source particles toward the Earth. Thus the plasmasphere is less eroded (from 59° to 57° at MLT = 18, i.e., the red lines) and the plasmapause is positioned at larger L shells, as shown in Figure 4g. As the hiss waves inside the plasmapause could scatter energetic electrons, an eastward-shifted plasmasphere plume leads to more energetic electron precipitation at dusk. This could explain the high-energy tail in the precipitating electron flux as shown in Figure 3g.

TIAN ET AL. 9 of 15

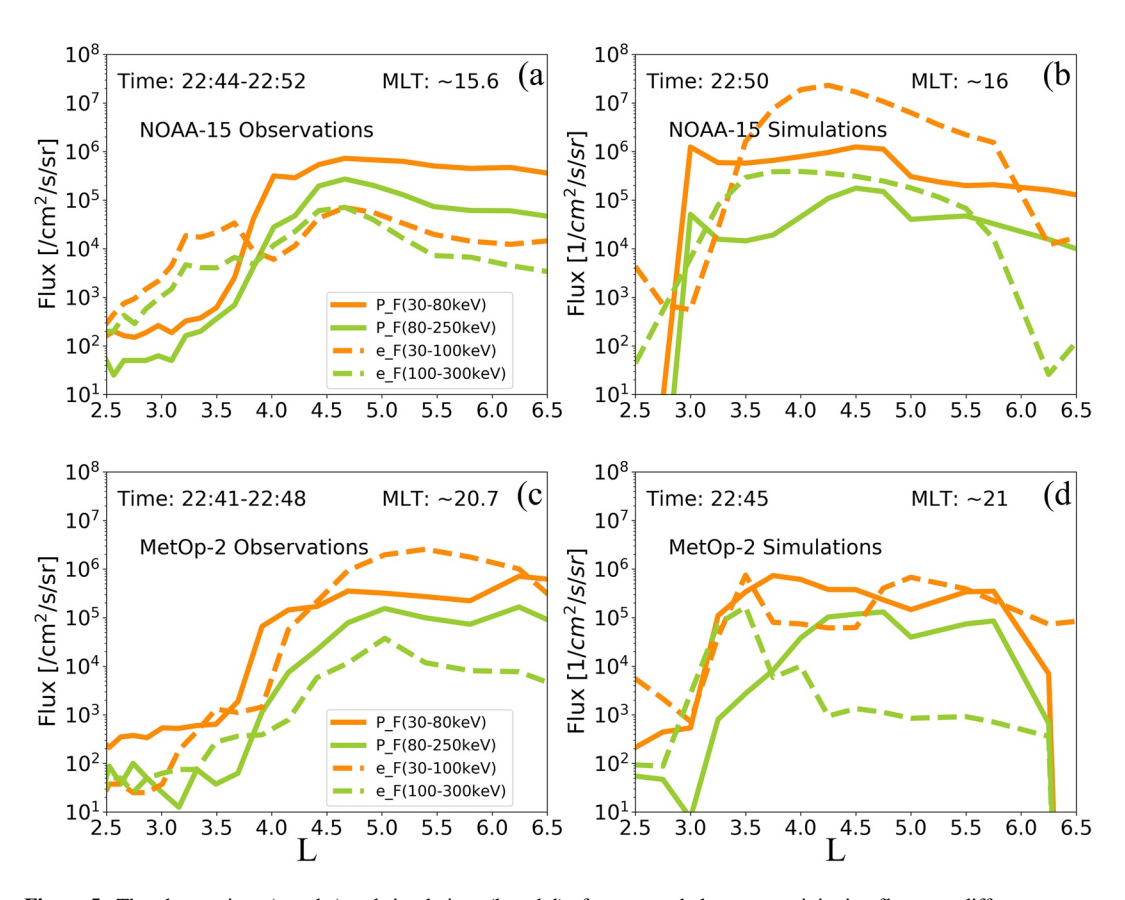


Figure 5. The observations (a and c) and simulations (b and d) of proton and electron precipitation flux over different energy ranges.

6. Comparisons With Observations

Lastly, we compare our simulation results to observations to validate and better understand the fidelity of the model. Figure 5 shows both simulated and observed precipitating flux along NOAA-15 and MetOp-02 spacecraft. Along the NOAA-15 satellite, the model captures the intensity of the proton flux of 30–80 keV for L > 4 regions. The proton flux of 80–250 keV (solid green line) is underestimated for L > 4 and the precipitating electron flux is overestimated for 3.5 < L < 5.5, resulting in a dominance of electron flux, which is opposite to the data. One reason for such discrepancies is probably because the wave models (both EMIC waves and chorus waves) used in this study are all statistics-based, which cannot precisely represent the wave activity at this moment and location. As for the flux along the MetOp-02 trajectory, the model reproduces the intensity of the precipitating proton flux at both energy channels (solid lines) for L > 3.7. The simulated electron flux is also comparable to the data for the energy channel of 30–100 keV. Like in the data, the precipitating proton flux in the model dominates the electron flux at the higher-energy channel and is comparable to the electron flux at the lower-energy channel. These similarities indicate a reasonable capability of the model in this region. Along both trajectories at lower L-shells (L < 3.7), the model predicts more precipitation than observations. The dropout boundary is closer to the Earth than in the data. This is probably caused by the under-shielding of the electric field in the current model (Shreedevi et al., 2021; Yu et al., 2015). Another possibility is that the statistical wave model suggests waves at much lower L-shells than in reality during this particular event. As shown in Figure 2, the EMIC wave amplitude implemented in the model is fairly strong in the noon-to-dusk sector even down to L=3, but the EMIC waves observed by the PINA and THRF ground-based stations occur around L = 4 at MLT = 16. We screened other stations at lower latitudes and found no EMIC wave activity, implying that the EMIC waves are not likely to occur at such small L-shell regions as low as L = 3.

We also compare the ionospheric electron density at mid-latitudes around 52°-55° where the Millstone Hill ISR is located. During this event, the radar data is only available during the daytime. Figure 6a shows an example

TIAN ET AL. 10 of 15



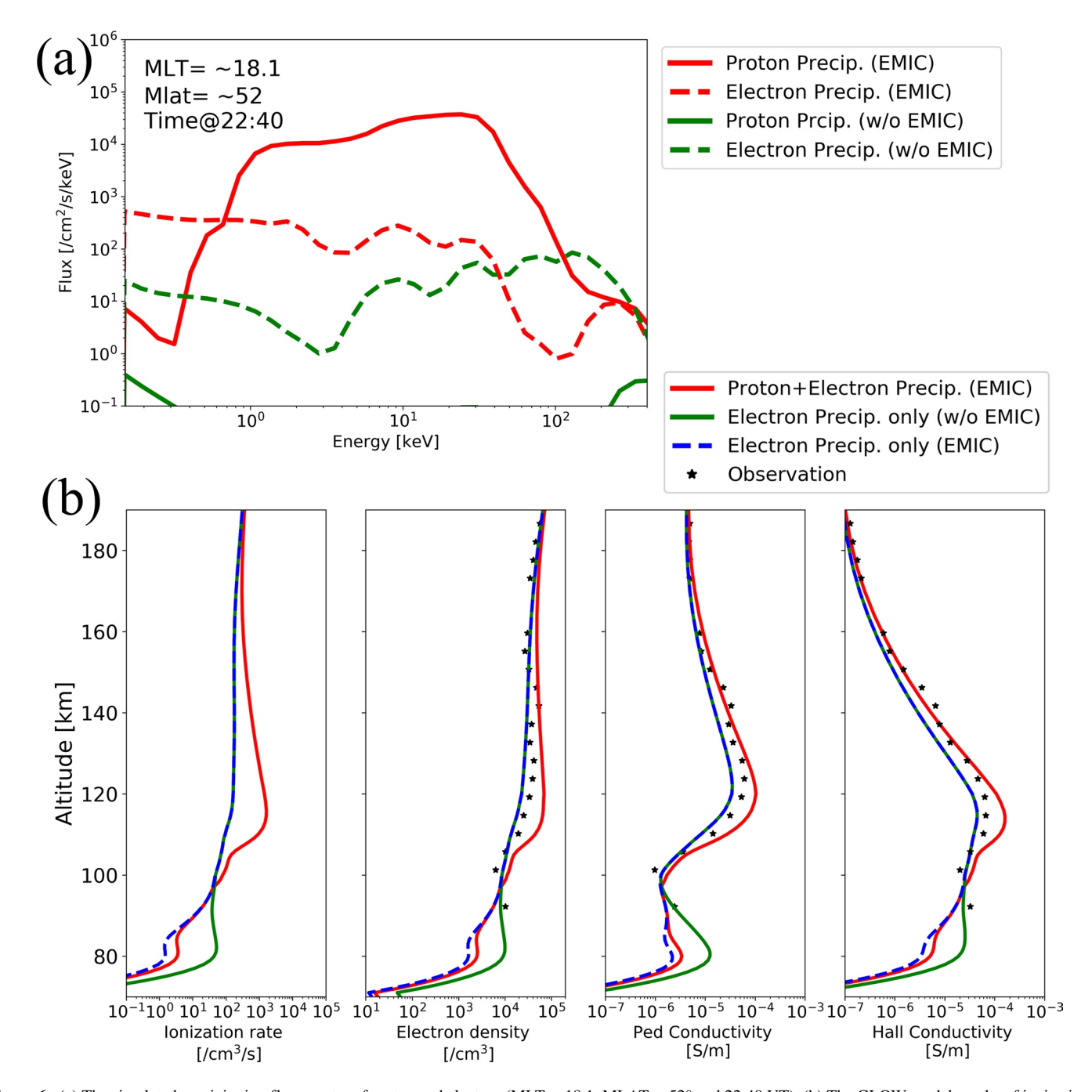


Figure 6. (a) The simulated precipitation flux spectra of proton and electron (MLT ~ 18.1 , MLAT $\sim 52^{\circ}$ and 22:40 UT). (b) The GLOW model results of ionization rate, electron density, Pedersen conductivity and Hall conductivity (red lines: The EMIC waves are considered and the incident particles contain both precipitating electrons and protons; green lines: The EMIC waves are not included and the incident particles are solely electrons; blue dashed line: The EMIC waves are considered and the incident particles contain only precipitating electrons; Black asterisk: observations from the Millstone Hill ISR).

of the simulated precipitating flux spectra of both protons and electrons at the Millstone Hill ISR location at 22:38 UT (at MLT ~ 18.1 and MLAT $\sim 52^{\circ}$). When the effect of EMIC waves is excluded, the precipitating electron flux (green dash line) is around $10^2/cm^2/s/keV$ for E > 5 keV, being the only particle precipitation source into the atmosphere. When the EMIC wave scattering is added, the electron flux (red dash line) enhances at lower energies (<5 keV) but decreases at higher energies (>40 keV). Such change of electron precipitation is due to the feedback effect within the coupled system, as discussed above. On the other hand, the proton precipitation enabled by the EMIC wave scattering is significantly enhanced at the radar location, about 1–2 orders of magnitude

TIAN ET AL.



larger than the electrons. Although the high-energy tail in the precipitating electron flux diminishes in this case, the proton precipitating flux spectrum is hard above 50 keV.

Shown in asterisks for comparisons are the observed electron density by the Millstone Hill ISR, and calculated Pedersen and Hall conductivities determined by the electron density data. When the EMIC waves are not included and the incident particles are solely electrons (green line), the F region electron density between 120 and 150 is slightly underestimated. When the EMIC waves are considered and the incident particles contain both precipitating electrons and protons (red line), the electron density in the F region is lifted, exceeding the data slightly. Both profiles show small disagreement from the observations. Overall, the GLOW model can capture the major characteristics of the ionosphere in the E/F regions. Although the photoionization remains as the main energy source of ionization with a solar elevation angle of 2.5° at the radar location, the impact of the EMIC wave-induced proton precipitation is still strong (red line). The simulated E/F region electron density is enhanced from 6.5×10^4 cm⁻³ to 7.2×10^4 cm⁻³ after the inclusion of the incident protons, amplifying the Pedersen conductivity from 3.5×10^{-5} S/m to 1.0×10^{-4} S/m at 120 km. These ionospheric parameters are enhanced by a factor of about 2-3.

7. Discussion and Summary

Electron precipitation is widely recognized as one of the major energy sources in the ionosphere, but recent studies found that the contribution of precipitating protons to the total energy deposition is also not negligible. How the ionosphere responds to the proton precipitation in a global context is still not fully understood and this is the main subject of this study. We report a proton precipitation event that occurred in the late storm main phase of the 17 March 2013 storm and simulated the global proton precipitation and subsequent responses in the ionosphere using a kinetic ring current model RAM-SCBE coupled with an ionospheric electron transport code GLOW.

After applying a statistical EMIC wave model to drive the proton scattering in the magnetosphere, we found that the EMIC wave diffusion process can result in significant precipitation of tens of keV protons in the noon-dusk sector near the plasmapause. In contrast, the electron precipitating flux at dusk is not as much. Through the GLOW model, we further investigated the height-dependent ionospheric responses. Driven by the EMIC waves, the tens of keV proton precipitation largely amplify the ionospheric electron density and conductivity in the E and F regions. On the other hand, energetic electrons in the high-energy tail of the precipitating spectrum cause the enhancement of the D region conductivity below 100 km. The integrated auroral conductance is significantly enhanced in the dusk-to-midnight sector. Interestingly, although the EMIC waves do not directly interact with the ring current electrons, after we included the EMIC wave scattering in the model, remarkable changes were found in the global distribution of precipitating electron flux. For example, the shape of the precipitating spectrum of electrons at dusk is changed after the inclusion of EMIC wave scattering in the simulation. This means that the addition of proton precipitation driven by EMIC waves results in feedback effects on the ring current electron dynamics through the circulation system. The convective electric potential is notably altered in the dusk sector, which further influences the drift velocity of magnetospheric particles and their precipitating loss. Our future studies will investigate these feedback effects in detail.

Comparisons with NOAA satellite measurements indicated that the model can roughly capture major features, such as the intensity of precipitating flux of tens of keV protons for L > 4. Along the MetOp-02 trajectory, the dominance of precipitating proton flux over electron flux was reproduced, but such a phenomenon was missed along the NOAA-15 satellite. The cause of disagreement may be a result of using statistical wave models as the averaged condition can be very different from the event-specific wave activity. Comparisons with Millstone Hill radar observations of electron density and derived conductivity at mid-latitudes suggested that the GLOW model, driven by the precipitating particles and EUV radiation, can reasonably well capture the altitudinal characteristics of the ionosphere. With the inclusion of EMIC wave-induced proton precipitation, the simulated electron density in the E/F region changed by a factor of 2–3. Given the strong photoionization at the radar location, the impact of proton precipitation only made the limited contribution. Overall, the simulation results showed good agreement with the data.

It should be noted that the resolution of our ring current model is \triangle MLT = 1 hr and \triangle L = 0.25 Re, so the global model is not able to capture the localized EMIC-wave particle interaction especially in the longitudinal dimension. On the other hand, a statistical distribution of the EMIC waves may not be suitable for a single event study,

TIAN ET AL. 12 of 15



as the statistics represents average conditions. In the future, we will consider increasing the model resolution to include smaller-scale physics and improve the model self-consistency by identifying the wave instability before incorporating the wave-particle interaction.

Data Availability Statement

The RAM-SCBE model code is available at https://github.com/lanl/RAM-SCB. The GLOWmodel code used in the study can be obtained at the HAO/NCARwebsite: https://www2.hao.ucar.edu. The simulation data is available at https://doi.org/10.5281/zenodo.5599674.

Acknowledgments

This work was supported by the National Natural Science Foundation of China grants 41974192 and 41821003. Simulations were performed on TianHe-2 at National Supercomputer Center in Guangzhou, China. The Millstone Hill ISR data is accessed through the MIT Haystack Observatory Madrigal database. The authors thank I.R. Mann, D.K. Milling and the rest of the CARISMA team for data, CARISMA is operated by the University of Alberta, funded by the Canadian Space Agency. The authors are also grateful to the NOAA website for providing POES data (http://satdat. ngdc.noaa.gov/sem/poes/). Work at Los Alamos was conducted under the auspices of the U.S. Department of Energy, with partial support from NSF grant IAA2027951.

References

- Albert, J. (2005). Evaluation of quasi-linear diffusion coefficients for whistler mode waves in a plasma with arbitrary density ratio. *Journal of Geophysical Research*, 110(A3). https://doi.org/10.1029/2004JA010844
- Bailey, S. M., Barth, C. A., & Solomon, S. C. (2002). A model of nitric oxide in the lower thermosphere. *Journal of Geophysical Research*, 107(A8). https://doi.org/10.1029/2001JA000258
- Bilitza, D., Altadill, D., Zhang, Y., Mertens, C., Truhlik, V., Richards, P., et al. (2014). The International Reference Ionosphere 2012—A model of international collaboration. *Journal of Space Weather and Space Climate*, 4, A07. https://doi.org/10.1051/swsc/2014004
- Cao, X., Ni, B., Liang, J., Xiang, Z., Wang, Q., Shi, R., et al. (2016). Resonant scattering of central plasma sheet protons by multib-and EMIC waves and resultant proton loss timescales. *Journal of Geophysical Research: Space Physics*, 121(2), 1219–1232. https://doi.org/10.1002/2015JA021933
- Chen, M. W., Lemon, C. L., Guild, T. B., Keesee, A. M., Lui, A., Goldstein, J., et al. (2015). Effects of modeled ionospheric conductance and electron loss on self-consistent ring current simulations during the 5–7 April 2010 storm. *Journal of Geophysical Research: Space Physics*, 120(7), 5355–5376. https://doi.org/10.1002/2015JA021285
- Chen, M. W., Lemon, C. L., Hecht, J., Sazykin, S., Wolf, R. A., Boyd, A., & Valek, P. (2019). Diffuse auroral electron and ion precipitation effects on RCM-E comparisons with satellite data during the 17 march 2013 storm. *Journal of Geophysical Research: Space Physics*, 124(6), 4194, 4216. https://doi.org/10.1039/201914032545
- 4194–4216. https://doi.org/10.1029/2019JA026545
 Chen, M. W., Lemon, C. L., Orlova, K., Shprits, Y., Hecht, J., & Walterscheid, R. L. (2015). Comparison of simulated and observed trapped and precipitating electron fluxes during a magnetic storm. *Geophysical Research Letters*, 42(20), 8302–8311. https://doi.org/10.1002/2015GL065737
- Chen, M. W., & Schulz, M. (2001). Simulations of diffuse aurora with plasmasheet electrons in pitch angle diffusion. Geophysical Research Letters, 106(A12), 28949–28966. https://doi.org/10.1029/2001JA000138
- Chen, M. W., Schulz, M., Anderson, P. C., Lu, G., Germany, G., & Wüest, M. (2005). Storm time distributions of diffuse auroral electron energy and X-ray flux: Comparison of drift-loss simulations with observations. *Journal of Geophysical Research*, 110(A3), A03210. https://doi.org/10.1029/2004JA010725
- Creutzberg, F., Gattinger, R., Harris, F., Wozniak, S., & Jones, A. V. (1988). Auroral studies with a chain of meridian scanning photometers, 2, Mean distributions of proton and electron aurora as a function of magnetic activity. *Journal of Geophysical Research*, 93(A12), 14591–14601. https://doi.org/10.1029/JA093iA12p14591
- Ebihara, Y., & Ejiri, M. (2003). Numerical simulation of the ring current. Space Science Reviews, 105(1-2), 377-452. https://doi.org/10.1023/A:1023905607888
- Ebihara, Y., Fok, M.-C., Immel, T., & Brandt, P. (2011). Rapid decay of storm time ring current due to pitch angle scattering in curved field line. Journal of Geophysical Research, 116(A3). https://doi.org/10.1029/2010JA016000
- Evans, D., & Greer, M. (2004). Polar Orbiting Environmental Satellite Space Environment Monitor-2: Instrument Descriptions and Archive Data Documentation, Technical Memorandum 93 (Vol. 93). Boulder: NOAAColorado OAR SEC.
- Fang, X., Lummerzheim, D., & Jackman, C. H. (2013). Proton impact ionization and a fast calculation method. *Journal of Geophysical Research: Space Physics*, 118(8), 5369–5378. https://doi.org/10.1002/jgra.50484
- Fang, X., Randall, C. E., Lummerzheim, D., Wang, W., Lu, G., Solomon, S. C., & Frahm, R. A. (2010). Parameterization of monoenergetic electron impact ionization. *Geophysical Research Letters*, 37(22). https://doi.org/10.1029/2010GL045406
- Fuselier, S. A., Gary, S. P., Thomsen, M. F., Claflin, E. S., Hubert, B., Sandel, B. R., & Immel, T. (2004). Generation of transient dayside subauroral proton precipitation. *Journal of Geophysical Research*, 109(A12), A12227. https://doi.org/10.1029/2004JA010393
- Galand, M., & Evans, D. (2000). Radiation damage of the proton meped detector on Poes (TIROS/NOAA) satellites.
- Galand, M., Fuller-Rowell, T., & Codrescu, M. (2001). Response of the upper atmosphere to auroral protons. *Journal of Geophysical Research*, 106(A1), 127–139. https://doi.org/10.1029/2000JA002009
- Galand, M., & Richmond, A. D. (2001). Ionospheric electrical conductances produced by auroral proton precipitation. *Journal of Geophysical Research*, 106(A1), 117–125. https://doi.org/10.1029/1999JA002001
- Glauert, S. A., Horne, R. B., & Meredith, N. P. (2014). Three-dimensional electron radiation belt simulations using the BAS Radiation Belt Model with new diffusion models for chorus, plasmaspheric hiss, and lightning-generated whistlers. *Journal of Geophysical Research: Space Physics*, 119(1), 268–289. https://doi.org/10.1002/2013JA019281
- Hardy, D. A., Gussenhoven, M., & Brautigam, D. (1989). A statistical model of auroral ion precipitation. *Journal of Geophysical Research*, 94(A1), 370–392. https://doi.org/10.1029/JA094iA01p00370
- Horne, R. B., Kersten, T., Glauert, S. A., Meredith, N. P., Boscher, D., Sicard-Piet, A., et al. (2013). A new diffusion matrix for whistler mode chorus waves. *Journal of Geophysical Research: Space Physics*, 118(10), 6302–6318. https://doi.org/10.1002/jgra.50594
- Hosokawa, K., & Ogawa, Y. (2010). Pedersen current carried by electrons in auroral D-region. Geophysical Research Letters, 37(18). https://doi.org/10.1029/2010GL044746
- Immel, T. J., Mende, S. B., Frey, H. U., Peticolas, L. M., Carlson, C. W., Gérard, J.-C., et al. (2002). Precipitation of auroral protons in detached arcs. Geophysical Research Letters, 29(11), 1519. https://doi.org/10.1029/2001GL013847
- Jordanova, V., Farrugia, C., Thorne, R., Khazanov, G., Reeves, G., & Thomsen, M. (2001). Modeling ring current proton precipitation by electromagnetic ion cyclotron waves during the May 14–16, 1997, storm. *Journal of Geophysical Research*, 106(A1), 7–22. https://doi.org/10.1029/2000JA002008

TIAN ET AL. 13 of 15



- Jordanova, V., Spasojevic, M., & Thomsen, M. (2007). Modeling the electromagnetic ion cyclotron wave-induced formation of detached subauroral proton arcs. *Journal of Geophysical Research*, 112(A8), https://doi.org/10.1029/2006JA012215
- Jordanova, V. K., Miyoshi, Y. S., Zaharia, S., Thomsen, M. F., Reeves, G. D., Evans, D. S., et al. (2006). Kinetic simulations of ring current evolution during the Geospace Environment Modeling challenge events. *Journal of Geophysical Research*, 111(A10), A11S10. https://doi. org/10.1029/2006JA011644
- Jordanova, V. K., Tu, W., Chen, Y., Morley, S. K., Panaitescu, A.-D., Reeves, G. D., & Kletzing, C. A. (2016). RAM-SCB simulations of electron transport and plasma wave scattering during the October 2012 "double-dip" storm. *Journal of Geophysical Research: Space Physics*, 121(9), 8712–8727. https://doi.org/10.1002/2016JA022470
- Jordanova, V. K., Zaharia, S., & Welling, D. T. (2010). Comparative study of ring current development using empirical, dipolar, and self-consistent magnetic field simulations. *Journal of Geophysical Research*, 115, A00J11. https://doi.org/10.1029/2010JA015671
- Jun, C.-W., Miyoshi, Y., Kurita, S., Yue, C., Bortnik, J., Lyons, L., et al. (2021). The characteristics of EMIC waves in the magnetosphere based on the Van Allen Probes and Arase observations. *Journal of Geophysical Research: Space Physics*, 126(6), e29001. https://doi. org/10.1029/2020JA029001
- Liang, J., Donovan, E., Ni, B., Yue, C., Jiang, F., & Angelopoulos, V. (2014). On an energy-latitude dispersion pattern of ion precipitation potentially associated with magnetospheric EMIC waves. *Journal of Geophysical Research: Space Physics*, 119(10), 8137–8160. https://doi. org/10.1002/2014JA020226
- Lotko, W., Smith, R. H., Zhang, B., Ouellette, J. E., Brambles, O. J., & Lyon, J. G. (2014). Ionospheric control of magnetotail reconnection. Science. 345(6193), 184–187. https://doi.org/10.1126/science.1252907
- Lui, A., Venkatesan, D., Anger, C., Akasofu, S.-I., Heikkila, W., Winningham, J., & Burrows, J. (1977). Simultaneous observations of particle precipitations and auroral emissions by the ISIS 2 satellite in the 19–24 MLT sector. *Journal of Geophysical Research*, 82(16), 2210–2226. https://doi.org/10.1029/JA082i016p02210
- Lyons, L. (1992). Formation of auroral arcs via magnetosphere-ionosphere coupling. Reviews of Geophysics, 30(2), 93–112. https://doi.org/10.1029/92RG00002
- Mann, I. R., Milling, D. K., Rae, I. J., Ozeke, L. G., Kale, A., Kale, Z. C., et al. (2008). The upgraded CARISMA magnetometer array in the THEMIS era. Space Science Reviews, 141(1-4), 413-451. https://doi.org/10.1007/s11214-008-9457-6
- McGranaghan, R., Knipp, D. J., Solomon, S. C., & Fang, X. (2015). A fast, parameterized model of upper atmospheric ionization rates, chemistry, and conductivity. *Journal of Geophysical Research: Space Physics*, 120(6), 4936–4949. https://doi.org/10.1002/2015JA021146
- Newell, P., Sotirelis, T., & Wing, S. (2009). Diffuse, monoenergetic, and broadband aurora: The global precipitation budget. *Journal of Geophysical Research*, 114(A9), A09207. https://doi.org/10.1029/2009JA014326
- Ni, B., Cao, X., Zou, Z., Zhou, C., Gu, X., Bortnik, J., et al. (2015). Resonant scattering of outer zone relativistic electrons by multiband EMIC waves and resultant electron loss time scales. *Journal of Geophysical Research: Space Physics*, 120(9), 7357–7373. https://doi. org/10.1002/2015JA021466
- Ni, B., Thorne, R. M., Zhang, X., Bortnik, J., Pu, Z., Xie, L., et al. (2016). Origins of the Earth's diffuse auroral precipitation. Space Science Reviews, 200(1-4), 205-259. https://doi.org/10.1007/s11214-016-0234-7
- Picone, J. M., Hedin, A. E., Drob, D. P., & Aikin, A. C. (2002). Nrlmsise-00 empirical model of the atmosphere: Statistical comparisons and scientific issues. *Journal of Geophysical Research*, 107(A12). https://doi.org/10.1029/2002ja009430
- Raeder, J., McPherron, R., Frank, L., Kokubun, S., Lu, G., Mukai, T., et al. (2001). Global simulation of the Geospace Environment Modeling substorm challenge event. *Journal of Geophysical Research*, 106(A1), 381–395. https://doi.org/10.1029/2000JA000605
- Ridley, A., Gombosi, T. I., & DeZeeuw, D. (2004). Ionospheric control of the magnetosphere: Conductance. *Annales Geophysicae*, 22, 567–584. https://doi.org/10.5194/angeo-22-567-2004
- Robinson, R., Vondrak, R., Miller, K., Dabbs, T., & Hardy, D. (1987). On calculating ionospheric conductances from the flux and energy of precipitating electrons. *Journal of Geophysical Research*, 92(A3), 2565–2569. https://doi.org/10.1029/JA092iA03p02565
- Saikin, A., Zhang, J.-C., Smith, C., Spence, H., Torbert, R., & Kletzing, C. (2016). The dependence on geomagnetic conditions and solar wind dynamic pressure of the spatial distributions of EMIC waves observed by the Van Allen Probes. *Journal of Geophysical Research: Space Physics*, 121(5), 4362–4377. https://doi.org/10.1002/2016JA022523
- Sakaguchi, K., Shiokawa, K., Miyoshi, Y., Otsuka, Y., Ogawa, T., Asamura, K., & Connors, M. (2008). Simultaneous appearance of isolated auroral arcs and Pc 1 geomagnetic pulsations at subauroral latitudes. *Journal of Geophysical Research*, 113(A5). https://doi.org/10.1029/2007JA012888
- Shreedevi, P., Yu, Y., Ni, B., Saikin, A., & Jordanova, V. K. (2021). Simulating the ion precipitation from the inner magnetosphere by H-band and He-band Electro Magnetic Ion Cyclotron (EMIC) waves. *Journal of Geophysical Research: Space Physics*, 126, e2020JA028553. https://doi.org/10.1029/2020JA028553
- Solomon, S. C. (2017). Global modeling of thermospheric airglow in the far ultraviolet. Journal of Geophysical Research: Space Physics, 122(7), 7834–7848. https://doi.org/10.1002/2017JA024314
- Su, Z., Gao, Z., Zheng, H., Wang, Y., Wang, S., Spence, H., et al. (2017). Rapid loss of radiation belt relativistic electrons by EMIC waves. *Journal of Geophysical Research: Space Physics*, 122(10), 9880–9897. https://doi.org/10.1002/2017JA024169
- Su, Z., Zong, Q.-G., Yue, C., Wang, Y., Zhang, H., & Zheng, H. (2011). Proton auroral intensification induced by interplanetary shock on 7 November 2004. *Journal of Geophysical Research*, 116(A8). https://doi.org/10.1029/2010JA016239
- Thorne, R. M., Ni, B., Tao, X., Horne, R. B., & Meredith, N. P. (2010). Scattering by chorus waves as the dominant cause of diffuse auroral precipitation. *Nature*, 467(7318), 943–946. https://doi.org/10.1038/nature09467
- Tian, X., Yu, Y., & Yue, C. (2020). Statistical survey of storm-time energetic particle precipitation. *Journal of Atmospheric and Solar-Terrestrial Physics*, 199, 105204. https://doi.org/10.1016/j.jastp.2020.105204
- Tsyganenko, N. A., & Sitnov, M. I. (2005). Modeling the dynamics of the inner magnetosphere during strong geomagnetic storms. *Journal of Geophysical Research*, 110(A3), A03208. https://doi.org/10.1029/2004JA010798
- Vasyliunas, V. M. (1970). Mathematical models of magnetospheric convection and its coupling to the ionosphere. In *Particles and fields in the magnetosphere* (pp. 60–71). Springer. https://doi.org/10.1007/978-94-010-3284-1_6
- Young, D. T., Balsiger, H., & Geiss, J. (1982). Correlations of magnetospheric ion composition with geomagnetic and solar activity. *Journal of Geophysical Research*, 87(A11), 9077–9096. https://doi.org/10.1029/JA087iA11p09077
- Young, S., Denton, R., Anderson, B., & Hudson, M. (2008). Magnetic field line curvature induced pitch angle diffusion in the inner magneto-sphere. *Journal of Geophysical Research*, 113(A3). https://doi.org/10.1029/2006JA012133
- Yu, Y., Jordanova, V., Zou, S., Heelis, R., Ruohoniemi, M., & Wygant, J. (2015). Modeling subauroral polarization streams during the 17 march 2013 storm. *Journal of Geophysical Research: Space Physics*, 120(3), 1738–1750. https://doi.org/10.1002/2014JA020371

TIAN ET AL. 14 of 15



- Yu, Y., Jordanova, V. K., McGranaghan, R. M., & Solomon, S. C. (2018). Self-consistent modeling of electron precipitation and responses in the ionosphere: Application to low-altitude energization during substorms. *Geophysical Research Letters*, 45(13), 6371–6381. https://doi. org/10.1029/2018GL078828
- Yu, Y., Jordanova, V. K., Ridley, A. J., Albert, J. M., Horne, R. B., & Jeffery, C. A. (2016). A new ionospheric electron precipitation module coupled with RAM-SCB within the geospace general circulation model. *Journal of Geophysical Research: Space Physics*, 121(9), 8554–8575. https://doi.org/10.1002/2016JA022585
- Yu, Y., Jordanova, V. K., Ridley, A. J., Toth, G., & Heelis, R. (2017). Effects of electric field methods on modeling the midlatitude ionospheric electrodynamics and inner magnetosphere dynamics. *Journal of Geophysical Research: Space Physics*, 122, 5321–5338. https://doi.org/10.1002/2016JA023850
- Yu, Y., Tian, X., & Jordanova, V. K. (2020). The effects of field line curvature (FLC) scattering on ring current dynamics and isotropic boundary. Journal of Geophysical Research: Space Physics, 125(8), e27830. https://doi.org/10.1029/2020JA027830
- Yuan, Z., Deng, X., Lin, X., Pang, Y., Zhou, M., Décréau, P., et al. (2010). Link between emic waves in a plasmaspheric plume and a detached sub-auroral proton arc with observations of cluster and image satellites. *Geophysical Research Letters*, 37(7). https://doi.org/10.1029/2010g1042711
- Yuan, Z., Xiong, Y., Li, H., Huang, S., Qiao, Z., Wang, Z., et al. (2014). Influence of precipitating energetic ions caused by EMIC waves on the subauroral ionospheric E region during a geomagnetic storm. *Journal of Geophysical Research: Space Physics*, 119(10), 8462–8471. https://doi.org/10.1002/2014JA020303
- Yuan, Z., Xiong, Y., Wang, D., Li, M., Deng, X., Yahnin, A. G., et al. (2012). Characteristics of precipitating energetic ions/electrons associated with the wave-particle interaction in the plasmaspheric plume. *Journal of Geophysical Research*, 117(A8), A08324. https://doi.org/10.1029/2012JA017783
- Zaharia, S., Jordanova, V. K., Thomsen, M. F., & Reeves, G. D. (2006). Self-consistent modeling of magnetic fields and plasmas in the inner magnetosphere: Application to a geomagnetic storm. *Journal of Geophysical Research*, 111(A10), A11S14. https://doi.org/10.1029/2006JA011619
- Zhang, B., Lotko, W., Brambles, O., Wiltberger, M., & Lyon, J. (2015). Electron precipitation models in global magnetosphere simulations. Journal of Geophysical Research: Space Physics, 120(2), 1035–1056. https://doi.org/10.1002/2014JA020615
- Zhu, M., Yu, Y., Tian, X., Shreedevi, P., & Jordanova, V. K. (2021). On the ion precipitation due to field line curvature (FLC) and EMIC wave scattering and their subsequent impact on the ionospheric electrodynamics. *Journal of Geophysical Research: Space Physics*, 126. https://doi.org/10.1029/2020JA028812

TIAN ET AL. 15 of 15